iScience

CellPress
OPEN ACCESS

Article

Doping of Sn-based two-dimensional perovskite semiconductor for high-performance field-effect transistors and thermoelectric devices

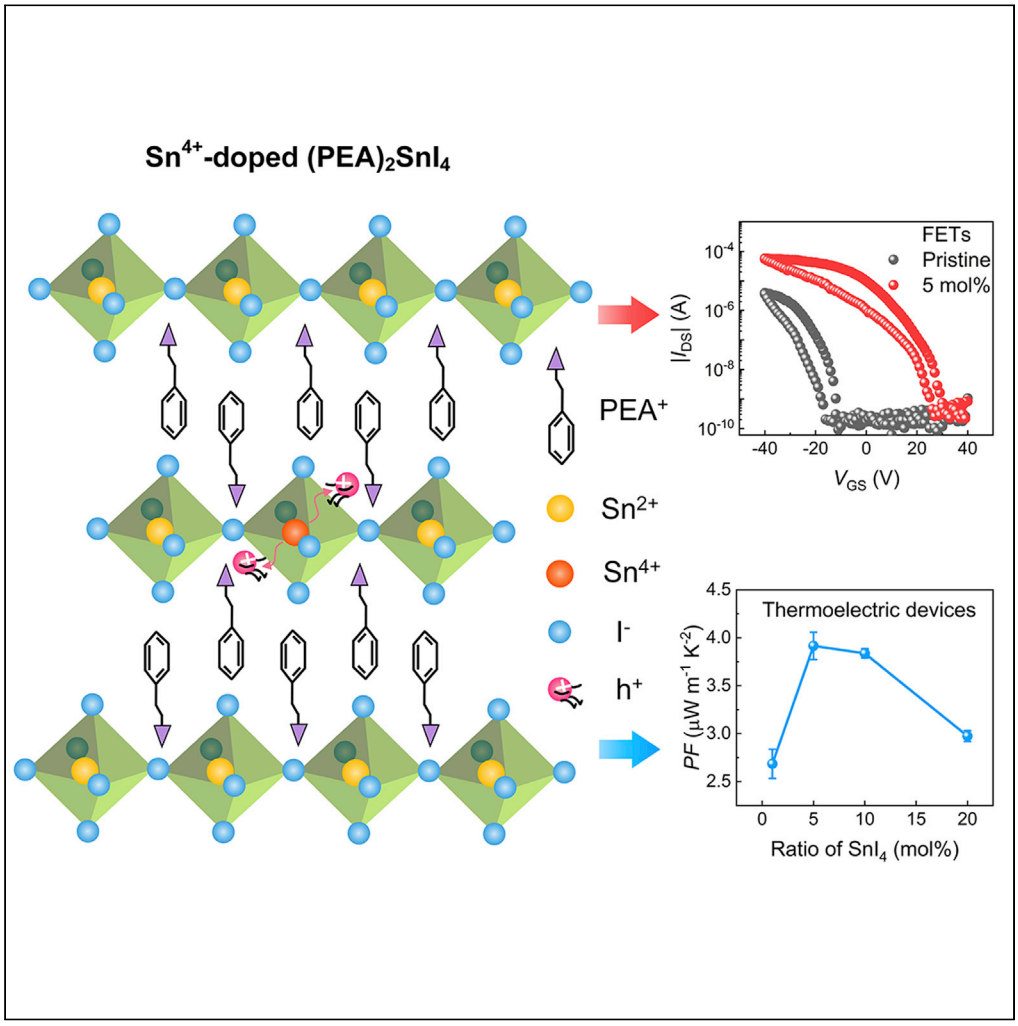

Yu Liu, Ping-An Chen, Xincan Qiu, ..., Lang Jiang, Lei Liao, Yuanyuan Hu

ljiang@iccas.ac.cn (L.J.)
yhu@hnu.edu.cn (Y.H.)

Highlights

The p-doping effect of Sn^{4+} on $(PEA)_2SnI_4$ is demonstrated and confirmed.

Proper Sn^{4+} doping can improve the mobilities of $(PEA)_2SnI_4$ FETs.

Thermoelectric performance of $(PEA)_2SnI_4$ is characterized and enhanced by Sn^{4+} doping.

Liu et al., iScience 25, 104109
April 15, 2022
https://doi.org/10.1016/j.isci.2022.104109

iScience

CellPress
OPEN ACCESS

Article

Doping of Sn-based two-dimensional perovskite semiconductor for high-performance field-effect transistors and thermoelectric devices

Yu Liu,[1,2] Ping-An Chen,[1] Xincan Qiu,[1] Jing Guo,[1] Jiangnan Xia,[1] Huan Wei,[1] Haihong Xie,[1] Shijin Hou,[1] Mai He,[1] Xiao Wang,[1] Zebing Zeng,[3] Lang Jiang,[4,*] Lei Liao,[1] and Yuanyuan Hu[1,2,5,*]

SUMMARY

Doping is an important technique for semiconductor materials and devices, yet effective and controllable doping of organic-inorganic halide perovskites is still a challenge. Here, we demonstrate a facile way to dope two-dimensional Sn-based perovskite $(PEA)_2SnI_4$ by incorporating SnI_4 in the precursor solutions. It is observed that Sn^{4+} produces p-doping effect on the perovskite, which increases the electrical conductivity by 10^5 times. The dopant SnI_4 is also found to improve the film morphology of $(PEA)_2SnI_4$, leading to reduced trap states. This doping technique allows us to improve the room temperature mobility of $(PEA)_2SnI_4$ field-effect transistors from 0.25 to 0.68 $cm^2\ V^{-1}\ s^{-1}$ thanks to reduced trapping effects in the doped devices. Moreover, the doping technique enables the characterization and improvement of the thermoelectric performance of $(PEA)_2SnI_4$ films, which show a high power factor of 3.92 $\mu W\ m^{-1}\ K^{-2}$ at doping ratio of 5 mol %.

INTRODUCTION

Organic-inorganic hybrid perovskite (OIHP) semiconductors have been extensively studied in the field of solar cells, light-emitting diodes, and photodetectors due to their excellent optoelectronic properties, such as large light-absorption coefficients, weakly bound excitons, long charge-carrier diffusion length, and tunable bandgap (García de Arquer et al., 2017; Liu et al., 2020; Ni et al., 2020; Wang et al., 2019b; Zhao et al., 2020). The low effective mass and intrinsically high carrier mobility of perovskite semiconductors also make them especially attractive as the semiconductor layers in field-effect transistors (FETs) (Senanayak et al., 2020; She et al., 2020; Wang et al., 2019a).

Among the various perovskite semiconductors, Sn-based two-dimensional (2D) layered perovskites have been the subject of interest for their promising applications in high-mobility FETs (Kagan et al., 1999; Matsushima et al., 2016; Zhu et al., 2020b). Compared to their three-dimensional (3D) analogs, 2D perovskite possesses good environmental stability because the bulky hydrophobic organic cationic chains between inorganic octahedral cages can prevent moisture and oxygen from intruding into the materials (Liu et al., 2021). Meanwhile, the ion migration causing the gate-field screening effect, which is believed to be a bottleneck for 3D perovskite FETs (Senanayak et al., 2017; Zeidell et al., 2018), is minimized in 2D perovskite since bulky organic chains can effectively inhibit the ion migration along the out-of-plane direction (Lin et al., 2017; Matsushima et al., 2016; Tsai et al., 2016). More interestingly, the organic ligands in 2D perovskites can be structurally engineered, which provides a paradigm for tuning the properties of perovskites through structure engineering (Gao and Dou, 2021; Gao et al., 2019a, 2019b; Liang et al., 2021). For example, Dou et al. demonstrated that the introduction of bulky conjugated organic ligands can enhance the stability as well as the carrier mobility of Sn-based 2D perovskites relative to short aliphatic chains (Gao et al., 2019b; Liang et al., 2021). As the most heavily studied Sn-based 2D perovskite, $(C_6H_5C_2H_4NH_3)_2SnI_4$ ($(PEA)_2SnI_4$) has attracted a lot of interest since the first report of $(PEA)_2SnI_4$ FETs with mobility of 0.6 $cm^2\ V^{-1}\ s^{-1}$ by Kagan et al., in 1999 (Kagan et al., 1999), and hole mobility as high as 15 $cm^2\ V^{-1}\ s^{-1}$ was reported in carefully designed $(PEA)_2SnI_4$ FETs (Matsushima et al., 2016), indicating the great potential of this semiconductor for flexible, printable, large-area and low-cost thin-film transistors.

[1]Key Laboratory for Micro/Nano Optoelectronic Devices of Ministry of Education & International Science and Technology Innovation Cooperation Base for Advanced Display Technologies of Hunan Province, School of Physics and Electronics, Hunan University, Changsha 410082, China

[2]Shenzhen Research Institute of Hunan University, Shenzhen 518063, China

[3]State Key Laboratory of Chemo/Biosensing and Chemometrics, College of Chemistry and Chemical Engineering, Hunan University, Changsha 410082, China

[4]Beijing National Laboratory for Molecular Sciences, Key Laboratory of Organic Solids, Institute of Chemistry, Chinese Academy of Sciences, Beijing 100190, China

[5]Lead contact

*Correspondence: ljiang@iccas.ac.cn (L.J.), yhu@hnu.edu.cn (Y.H.)

https://doi.org/10.1016/j.isci.2022.104109

As well known, doping is an essential technique for semiconductors and devices since it can provide efficient adjustment to the electrical properties of semiconductors in terms of carrier concentration and mobility. As a typical example of doping, silicon doping takes the form of atomic substitution by thermal diffusion or ion implantation and now is an indispensable technique in the modern microelectronics industry. Doping has also been intensively studied in organic semiconductor counterparts due to the great potential benefits that can be brought by the technique (Guo et al., 2021; Jacobs and Moule, 2017; Sakai et al., 2021; Wei et al., 2021; Yamashita et al., 2019). Being an emerging semiconductor, $(PEA)_2SnI_4$ provides new opportunities and platforms for studying doping physics and techniques, which will not only help enhance the performance of $(PEA)_2SnI_4$ FETs but also expand its applications in other optoelectronic devices.

Previously, Qin et al. reported the substitutional doping of $(PEA)_2SnI_4$ by Pb^{2+}, which leads to improved environmental stability of $(PEA)_2SnI_4$ FETs but depressed hole transport owing to the larger effective mass of Pb and higher contact resistance in the devices (Qin et al., 2021). Reo et al. considered doping of $(PEA)_2SnI_4$ thin films with Cu^+ by adding copper iodide (CuI) in the precursor solution (Reo et al., 2021). It turns out that the hole transport in $(PEA)_2SnI_4$ FETs gets enhanced with the incorporation of CuI. However, further density functional theory (DFT) calculations and X-ray diffraction (XRD) measurements reveal that the Cu^+ is likely distributed at grain boundaries instead of replacing the Sn^{2+} within the perovskite lattices, and the improved FET performance is more likely attributed to the outstanding hole-transport property of CuI rather than doping (Reo et al., 2021). These studies indicate doping can be a powerful technique to tune or enhance the performance of $(PEA)_2SnI_4$ devices, but presently effective doping strategies for $(PEA)_2SnI_4$ remain to be established.

Herein, we report effective p-doping of $(PEA)_2SnI_4$ 2D layered perovskite with Sn^{4+} through substituting part of the SnI_2 with SnI_4 in the precursor solution. The doping effect of Sn^{4+} was confirmed by electrical and spectroscopy characterizations. In addition to the doping effect, the incorporation of SnI_4 was revealed to improve the film morphology of $(PEA)_2SnI_4$. This doping strategy was then used to fabricate bottom-gate bottom-contact (BGBC) $(PEA)_2SnI_4$ FETs, which leads to an increase of average mobility from 0.25 $cm^2\ V^{-1}\ s^{-1}$ for pristine devices to 0.68 $cm^2\ V^{-1}\ s^{-1}$ for devices doped with 5 mol % SnI_4. The effect of doping on charge injection and charge transport processes in the FET devices are also investigated and clarified. Moreover, the doping technique allows us to characterize the thermoelectric (TE) performance of $(PEA)_2SnI_4$, and Seebeck coefficients varying between 387 and 660 $\mu V\ K^{-1}$ were observed, with the maximum power factor reaching 3.92 $\mu W\ m^{-1}\ K^{-2}$, which demonstrates the promising usage of 2D perovskite semiconductors for high-performance TE devices. It is notable that a similar doping strategy was reported in $(4Tm)_2FASn_2I_7$ for high-performance TE devices during the preparation of this manuscript (Hsu et al., 2021), which together with this study highlights the great potential of the SnI_4-doping technique to be used in 2D Sn-based perovskite for low-cost and high-performance devices.

RESULTS AND DISCUSSION

Doping of $(PEA)_2SnI_4$ films by SnI_4

Figure 1A illustrates the structure of $(PEA)_2SnI_4$, in which the corner-sharing $[SnI_6]^{4-}$ octahedra are alternated by a bilayer of PEA^+ organic cations. Previously, it was reported that Sn^{2+} in Sn-based perovskites are easily oxidized to Sn^{4+}, which are metastable and can thermodynamically evolve to the Sn^{2+}, releasing two holes in the valence band and leading to the p-doping of the perovskite, *i.e.*, $Sn^{4+} \rightarrow Sn^{2+} + 2h^+$ (Hsu et al., 2021; Ricciarelli et al., 2020; Stoumpos et al., 2013). These results motivate us to intentionally incorporate Sn^{4+} into $(PEA)_2SnI_4$ for controllable p-doping. For such purpose, Sn^{4+} was introduced by mixing phenethylammonium iodide (PEAI), SnI_2 and SnI_4 with mol ratio of $2:1-x:x$ ($0 < x < 1$) in a mixture of dimethylformamide (DMF) and N-Methyl-2-pyrrolidone (NMP) with volume ratio of 3:1, where x represents the doping ratio of SnI_4.

The measured electrical conductivities (σ) of $(PEA)_2SnI_4$ films doped with different doping ratios are shown in Figure 1C (see Figure S1 for more information), with the current-voltage curves shown in Figure 1B. The electrical conductivity of the pristine film is 2.6×10^{-6} S cm^{-1}, and it is enhanced as the doping ratio increases, reaching a maximum value of 2.1×10^{-1} S cm^{-1} at the doping ratio of 30 mol %, which is direct evidence showing the doping effect of SnI_4 on $(PEA)_2SnI_4$ perovskite. It should be mentioned that extra I^- was also introduced into the films together with Sn^{4+}, and I^- was reported to greatly improve the charge transport property of $(PEA)_2SnI_4$ by compensating the iodine vacancies (V_I), which behave as trap states (Reo et al., 2021). So, it might be argued that I^- may also contribute to the enhancement of conductivity in the doped $(PEA)_2SnI_4$ films. However, the dramatic increase of conductivity about five orders of

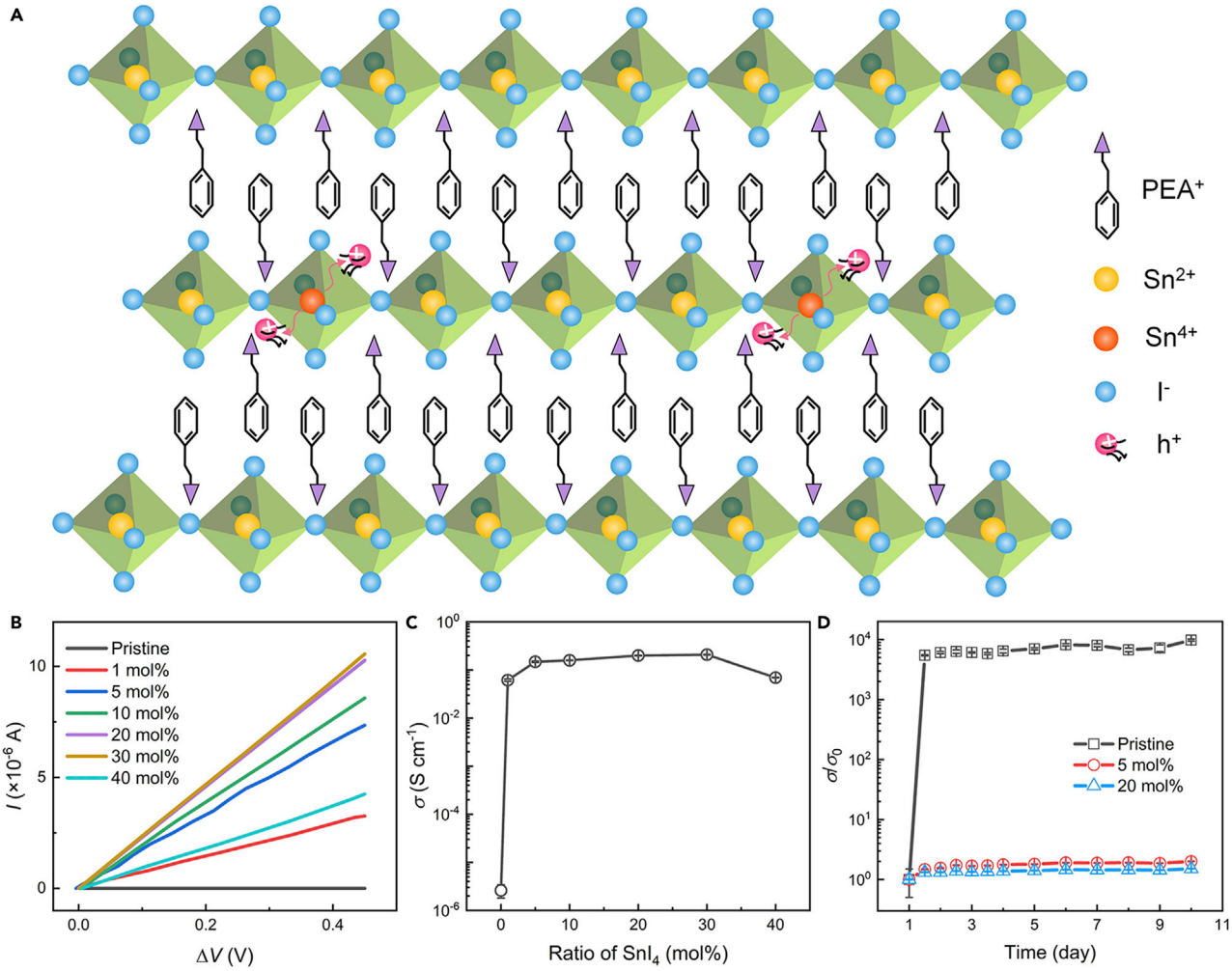

Figure 1. Confirmation of the doping effect of SnI_4 on $(PEA)_2SnI_4$

(A) Schematic diagram showing the structure of $(PEA)_2SnI_4$ and the SnI_4 doping mechanism.

(B) Current-voltage curves of perovskite films with different SnI_4 ratios.

(C) Electrical conductivities as a function of doping ratio calculated from (B).

(D) The relative conductivity changes (σ/σ_0) of pristine, 5 mol % and 20 mol % SnI_4-doped films with time when they were stored in Ar glove box.

magnitude in doped films suggests that it should be Sn^{4+} (doping effect) rather than I^- (trap passivation effect) that plays a dominant role. We then investigated the stability of the doped $(PEA)_2SnI_4$ films, with the results of relative conductivity changes (σ/σ_0) shown in Figure 1D, where σ_0 is the initial conductivity. It is seen that compared to the pristine $(PEA)_2SnI_4$ films, which are prone to be oxidized ($Sn^{2+} \rightarrow Sn^{4+}$) and experience conductivity increase even though they are stored in an Ar-filled glove box (Zhu et al., 2020b), the doped $(PEA)_2SnI_4$ films show better stability of the conductivity.

Structural and spectroscopic characterizations on doped $(PEA)_2SnI_4$ films

To further understand the doping effect of SnI_4 on $(PEA)_2SnI_4$ films, X-ray photoelectron spectroscopy (XPS) was used to identify the composition of Sn element in the perovskite films. Figure 2A demonstrates the XPS spectra of Sn 3d for pristine and 20 mol % SnI_4-doped $(PEA)_2SnI_4$ films. We find that the Sn^{4+} content of the doped $(PEA)_2SnI_4$ films is increased from 28 atomic % (at %) (for pristine ones) to 42 at % (for 20 mol%-doped ones), indicating the incorporation of Sn^{4+} during the film formation. Furthermore, UV photoelectron spectroscopy (UPS) measurements were performed to study the effects of doping on energy levels of perovskite films (Figure 2B). The Fermi level (E_F), valence band maximum (VBM), and conduction band minimum (CBM) for pristine films and films doped with 1 mol % and 5 mol % SnI_4 are shown in Figure 2C. The optical

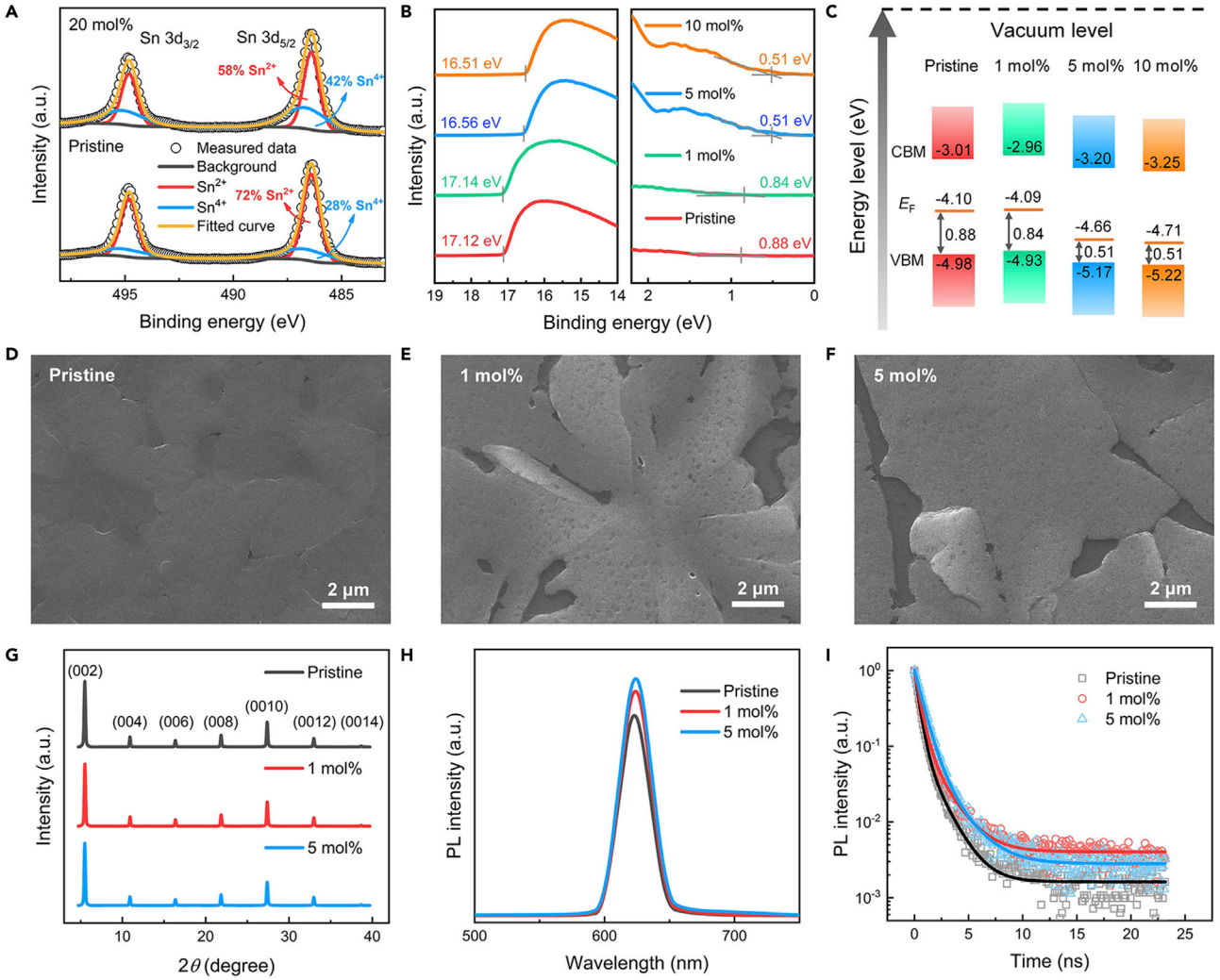

Figure 2. Characterizations of the doping effect of SnI_4 on $(PEA)_2SnI_4$

(A) XPS results of Sn 3d for pristine and 20 mol % SnI_4-doped $(PEA)_2SnI_4$ films. The fitting results of the peaks are illustrated in the figure, which show the ratio changes of SnI_4 upon doping.

(B) UPS results of pristine, 1, 5, and 10 mol % SnI_4-doped perovskite films.

(C–F) (C) Energy level structures of pristine, 1, 5, and 10 mol % SnI_4-doped perovskite films. SEM images of (D) pristine $(PEA)_2SnI_4$ films, (E) 1 mol %, and (F) 5 mol % SnI_4-doped $(PEA)_2SnI_4$ films (scale bar: 2 μm).

(G–I) (G) XRD patterns, (H) steady-state PL, and (I) time-resolved PL of $(PEA)_2SnI_4$ thin films with different doping ratios.

bandgap (E_g) for all the films were measured to be about 1.97 eV through absorption spectra (see more details in the Figure S2), which is consistent with the previously reported values (Zhang et al., 2021). One important result of UPS measurements is that the Fermi level moves closer to the VBM as the doping ratio increases, indicating the increased concentration of holes upon SnI_4 doping. We also note that the shifting of Fermi level becomes almost saturated when the doping ratio is higher than 5 mol %, which is in line with the saturation of electrical conductivity above this doping ratio as shown in Figure 1C.

Furthermore, we inspected the influence of SnI_4 on the morphology and structure of $(PEA)_2SnI_4$ films. From scanning electron microscopy (SEM) images of the perovskite films, it is seen that the domain is enlarged upon the SnI_4 doping (Figures 2D–2F), which is an indication of fewer domain boundaries and trap states. The corresponding atomic force microscopy (AFM) images also exhibit more uniform surface morphology with reduced roughness as doping ratio increases (Figure S3). To further understand the effect of SnI_4 on film structure, we used X-ray diffraction (XRD) to probe the film crystallinity. As shown in Figure 2G, XRD

patterns of pristine and doped $(PEA)_2SnI_4$ films show similar diffraction peaks, which are assigned to the strong (0 0 *l*) (*l* = 2, 4, 6, 8, 10, 12, 14) diffractions at 5.5°, 10.9°, 16.4°, 21.9°, 27.4°, 33.0°, and 38.7°, respectively, indicating a layered structure of the films (Reo et al., 2021; Zhu et al., 2020a). However, the full width at half maximum (FWHM) of (0 0 2) peaks are found to be 0.197°, 0.183°, and 0.182° for pristine, 1 mol %, and 5 mol % SnI_4-doped films, respectively. This decreased FWHM implies a larger crystallite size in doped films, which is in accordance with the SEM results.

In addition, we measured the steady-state and time-resolved photoluminescence (PL) spectra of $(PEA)_2SnI_4$ films prepared with and without SnI_4 dopants. From the steady-state PL spectra (Figure 2H), it is evident that the quenching of the perovskite emission signal is reduced in doped films, suggesting there are fewer traps causing non-radiative recombination. The time-resolved PL data (Figure 2I) are found to fit well to the biexponential decay equation:

$$I(t) = A_1 \exp\left(-\frac{t}{\tau_1}\right) + A_2 \exp\left(-\frac{t}{\tau_2}\right) \quad \text{(Equation 1)}$$

where A_1 and A_2 are relative amplitudes, τ_1 and τ_2 are carrier lifetimes for fast and slow decay, respectively, and $I(t)$ is the PL intensity (Bi et al., 2016). The carrier lifetimes of τ_1 (τ_2) for the pristine films and films doped with 1 mol % and 5 mol % SnI_4 are 0.40 ns (1.46 ns), 0.50 ns (1.74 ns), and 0.72 ns (2.10 ns), respectively. The longer PL lifetime of doped $(PEA)_2SnI_4$ films further demonstrates that the addition of SnI_4 can reduce the trap density in the films, consistent with the results of steady-state PL. Such reduction of trap density in the SnI_4-doped films is not unexpected since both the filling of trap states by dopants and improved crystallinity and morphology of the doped films can lower the trap density.

Doping of $(PEA)_2SnI_4$ films for FETs

Encouraged by the prominent doping effect of SnI_4 on $(PEA)_2SnI_4$ films and the accompanied improvement of film quality, we sought to lever these benefits to enhance the device performance of $(PEA)_2SnI_4$ FETs. Figure 3A shows the BGBC device structure used in this study. Si^{++}/SiO_2 (300 nm) were used as substrates, and photolithography-defined Cr/Au (2 nm/30 nm) were used as source/drain electrodes. Perovskite precursors were spin-coated on the substrates at 4000 rpm for 30 s and then annealed at 100°C for 10 min in a glove box. The devices with pristine $(PEA)_2SnI_4$ films as active layers show typical p-type FET behaviors due to the low formation energy of tin vacancies which can lead to self-doping effect (see Figure 3B) (Euvrard et al., 2021; Takahashi et al., 2011). The transfer plots (square root of current) for mobility calculations are shown in Figure S5A. The saturation mobility (μ) of 0.25 $\pm$ 0.08 $cm^2\ V^{-1}\ s^{-1}$, threshold voltage (V_{TH}) of −21 $\pm$ 1.6 V, and on/off ratio (I_{on}/I_{off}) of 10^4 (channel length L = 160 μm, channel width W = 1000 μm) were obtained in the devices, as shown in Figure 3C. These performance merits are similar to those reported in previous studies (Qin et al., 2021; Zhang et al., 2019; Zhu et al., 2020b).

By doping the films with SnI_4 in the doping range of 1–5 mol %, we observed a significant enhancement of the device current, indicating the improvement of device performance. However, the current begins to decay when the doping ratio is higher than 10 mol % (Figures 3B and S4). The variation of performance parameters as a function of doping ratio is presented in Figure 3C, which shows the devices exhibit μ of 0.68 $\pm$ 0.16 $cm^2\ V^{-1}\ s^{-1}$, V_{TH} of 10 $\pm$ 5.6 V, and I_{on}/I_{off} of 10^5 at the optimized doping ratio of 5 mol %. In addition, the doping-ratio-dependent carrier concentration (p) (see Figure S6) calculated from the formula $\sigma = pq\mu$, where q is the unit charge, exhibits a much higher σ upon doping with 1 mol % SnI_4 and a saturation trend with higher doping ratios. The output curves of the pristine and 5 mol % SnI_4-doped devices are shown in Figures 3D and 3E, respectively, and output curves of 1 mol % and 10 mol % SnI_4-doped devices are shown in Figures S5B and S5C. Thus, we can see that the currents of output curves increase in FETs with higher doping ratios. One thing notable is the increased hysteresis in the doped device, which is probably attributed to the extra I^- brought by SnI_4 in the films, causing enhanced ion migration. In spite of the slightly increased hysteresis, these results still show that doping $(PEA)_2SnI_4$ films with SnI_4 is a promising way to achieve high-performance FETs.

Following that, we conducted investigations to deeply understand how the doping affects the performance of $(PEA)_2SnI_4$ FETs. First, we examined the influence of doping on contact resistance (R_CW) in the devices through the transmission line method (TLM) (Bhargava and Singh, 2014; Minari et al., 2006; Xu et al., 2010). As shown in Figure 3F, the contact resistance for pristine devices is 9.6 × 10^4 Ω cm, and it is reduced to 1.2 × 10^4 Ω cm for the 5 mol % SnI_4-doped devices. The average total resistance (R_TW) of pristine and 5

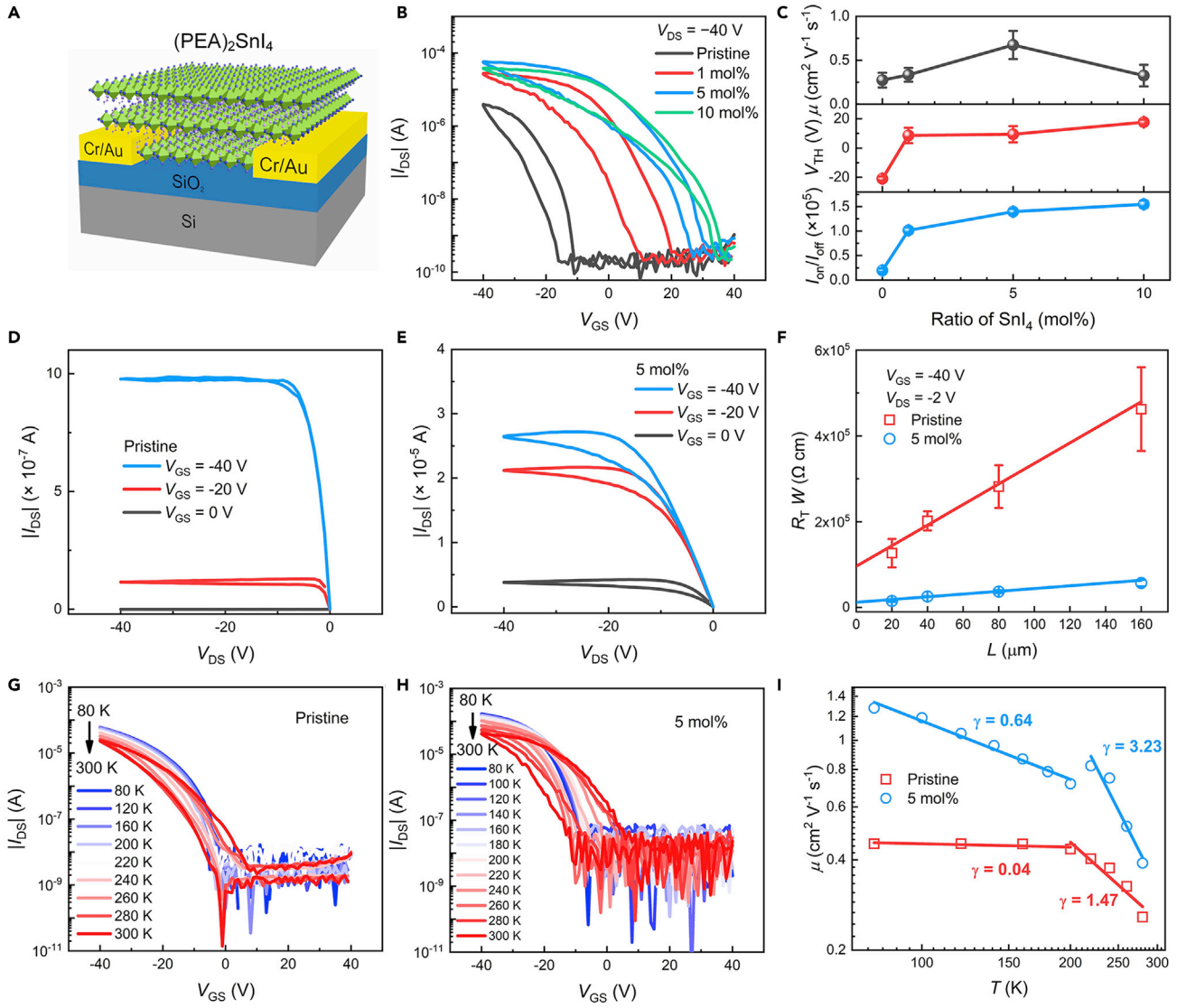

Figure 3. Fabrication and characterization of $(PEA)_2SnI_4$ FETs

(A) Device configuration of $(PEA)_2SnI_4$ BGBC FET.

(B) Transfer curves (V_{DS} = −40 V) of FETs with different doping ratios.

(C–E) (C) Mobilities, threshold voltages, and on/off ratios extracted from transfer characteristics. Output curves of the (D) pristine and (E) 5 mol % SnI_4-doped devices.

(F–H) (F) The L-dependent total resistance (R_TW) of pristine and 5 mol % SnI_4-doped FETs. Temperature-dependent FETs transfer characteristics of (G) pristine FETs and (H) 5 mol % SnI_4-doped FETs from 80 K to 300 K.

(I) Temperature-dependent mobility extracted from the transfer curves of pristine and 5 mol % SnI_4-doped FETs.

mol % SnI_4-doped FETs with L = 160 μm are 4.6 × 10^5 Ω cm and 5.7 × 10^4 Ω cm, respectively, by which the average channel resistance ($R_{Ch}W = R_TW - R_CW$) are obtained to be 3.6 × 10^5 Ω cm and 4.5 × 10^4 Ω cm, respectively. Interestingly, the ratio of R_CW of FETs before and after doping is about 8.0, which is similar to that of $R_{Ch}W$, indicating that doping has similar effects on R_CW and $R_{Ch}W$. The reduction of contact resistance and channel resistance are expected when doping of the semiconductor layer occurs in FETs (Hu et al., 2018a, 2018b; Kim et al., 2016, 2019).

Additionally, we inspected the charge transport in the pristine and doped devices by performing temperature-dependent measurements on their electrical characteristics (L = 80 μm, W = 2000 μm). It should be noted that the transfer curves of pristine and 5 mol % SnI_4-doped FETs change after vacuuming, as shown in

Figure S7. With the temperature increasing from 80 K to 300 K, the pristine device exhibits reduced I_{on} (at $V_G = -40$ V) and increased hysteresis (see Figure 3G). The cooling process from 300 K to 80 K also shows the same trend (see Figure S8). This increase of hysteresis is possibly attributed to the enhanced ion migration in the high-temperature regime although 2D perovskites have been reported to show inhibited ion migration compared to their 3D analogs (Liu et al., 2021). The extracted mobility and its temperature dependence are presented in Figure 3I, which illustrates an increase of μ with decreasing temperature. In general, the temperature dependence of charge-carrier mobility is closely related to the charge scattering mechanism in the semiconductors and can be expressed as $\mu \propto T^{-\gamma}$ (Biewald et al., 2019; Wright et al., 2016), where γ reflects the magnitude of charge scattering, with larger γ representing stronger scattering in the perovskite (Buizza et al., 2021; Herz, 2017; Senanayak et al., 2017). The pristine device shows a γ value of 1.47 between 200 and 280 K, which seems to indicate the charge transport in this regime is dominated by acoustic phonon scattering (Biewald et al., 2019; Wright et al., 2016; Yi et al., 2016). Nevertheless, the influence of ion migration cannot be fully excluded in this regime (Yi et al., 2016). At lower temperatures, the mobility becomes almost independent on temperature, with γ being 0.04. The transition of the μ-T relationship at T = 200 K is suspected to be caused by the phase transition of $(PEA)_2SnI_4$ films, as discussed in the following. The weak temperature dependence of mobility was frequently reported in polycrystalline FETs, which was accounted by the combined effect of charge-carrier trapping at grain boundaries and phonon scattering in the grains (Katoh, 1994). This explanation may be applicable to the $(PEA)_2SnI_4$ films because of their polycrystalline nature but remains to be further investigated.

By comparison, the 5 mol % SnI_4-doped devices present larger hysteresis (Figure 3H), which is probably due to the extra I^- brought by the SnI_4 adding, as mentioned earlier. Interestingly, the mobility of the doped device shows a larger γ value of 3.23 in the range of 200–280 K. This large γ value is comparable to the ones observed in $MAPbI_3$ FETs reported by Sirringhaus et al., which was believed to be accounted by ion migration (Senanayak et al., 2017). Thus, the larger γ in this regime suggests the more severe ion migration of the doped films, consistent with the more significant hysteresis shown earlier. In addition, an abrupt step change of mobility was seen at T = 200 K, which was reported to reflect the phase change of perovskite by Duan et al. (Yi et al., 2016). However, direct evidence showing the phase change of $(PEA)_2SnI_4$ films remains for further investigations, which is beyond the scope of this work. At $T < 200$ K, the μ keeps increasing as the T lowers, with γ being 0.64. Ion migration effect is not likely to account for this mobility increase because it is effectively suppressed at such low temperatures (Senanayak et al., 2017); however, the dominant mechanisms governing charge transport in this regime are not fully clear yet.

Doping of $(PEA)_2SnI_4$ films for TE devices

Although the investigation of OIHP-based TE devices is still in its infancy and lags much behind that of traditional inorganic and organic TE devices, their advantages of cost-effectiveness as well as inherently ultralow thermal conductivity (κ) and high Seebeck coefficient (S) make OIHPs promising TE materials (Filippetti et al., 2016; Haque et al., 2020b; Shukla et al., 2020). Two-dimensional OIHPs possess even lower κ than their 3D counterparts (Giri et al., 2020), partly because the large acoustic mismatch between the organic and inorganic layers in 2D OIHPs was found to suppress the acoustic phonon transport (Guo et al., 2018). These electronic and thermal properties of 2D OIHPs are beneficial for achieving a high TE figure of merit (ZT) = $S^2\sigma T/\kappa$, where σ is the electrical conductivity and T is the absolute temperature. However, similar to organic semiconductors, the inherent carrier concentration and electrical conductivity in 2D OIHPs is rather low, which not only poses challenges for the characterization of their TE performance but also hinders the achievement of large power factor (PF, $PF = S^2\sigma$) values (Cohen et al., 2017; Haque et al., 2020b; Mitzi et al., 1995). Here, with the doping technique shown earlier, we are allowed to evaluate the TE performance of $(PEA)_2SnI_4$ films by enhancing their σ values.

Figure 4A shows the schematic diagram of our setup for TE characterizations, which can provide information about S by measurements of temperature differences (ΔT) and the corresponding thermal voltages (ΔV) of the samples (see more information in the Method Details) (Wei et al., 2021). As shown in Figure 4B, ΔV becomes smaller with the increasing doping ratio at the same ΔT, indicating lower S (= $\Delta V/\Delta T$) at a higher doping ratio. Figure 4C shows the variation of TE parameters of $(PEA)_2SnI_4$ films with the doping ratio ranging from 1 mol % to 20 mol %. The average S extracted from Figure 4B reduced from 660 $\mu V\ K^{-1}$ to 387 $\mu V\ K^{-1}$, and the σ measured by the four-point probe method increased from 0.06 S cm^{-1} to 0.20 S cm^{-1}. The TE characterizations of pristine devices were not conducted due to their low electrical conductivities. The highest PF value we have achieved is about 3.92 $\mu W\ m^{-1}\ K^{-2}$ at the

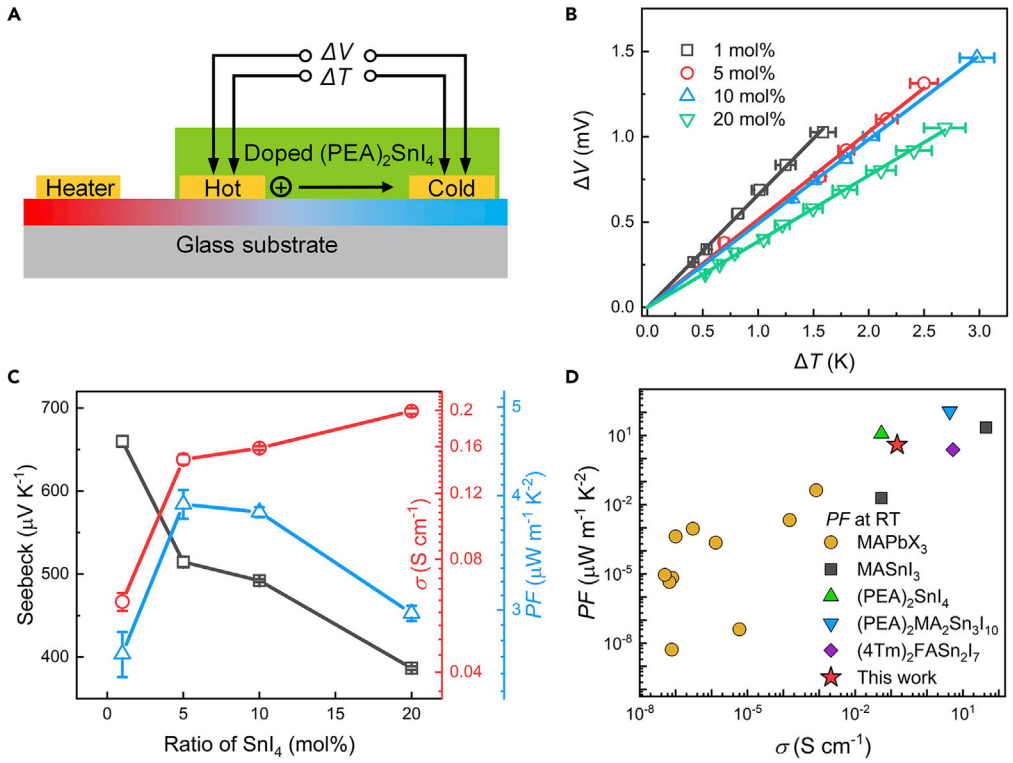

Figure 4. Thermoelectrical characterizations of doped $(PEA)_2SnI_4$ films

(A) The schematic diagram of the thermoelectric measurements.

(B) The dependence of thermal voltages on temperature differences for SnI_4-doped $(PEA)_2SnI_4$ films.

(C) Seebeck coefficients, electrical conductivities, and power factors of $(PEA)_2SnI_4$ films with different doping ratios.

(D) A summary of the *PF* values versus corresponding electrical conductivities of 3D and 2D OIHP semiconductors at room temperature (X denotes the halide ions).

doping ratio of 5 mol %. A summary of previously reported *PF* values as a function of electrical conductivities for 3D and 2D OIHP semiconductors at room temperature (RT), including $MAPbX_3$ (X denotes the halide ions) (Haque et al., 2019; Long et al., 2019; Mettan et al., 2015; Tang et al., 2020; Wu et al., 2018; Xie et al., 2021; Xiong et al., 2019; Ye et al., 2017), $MASnI_3$ (Hao et al., 2014; Haque et al., 2020a), $(PEA)_2MA_2Sn_3I_{10}$ (Yang et al., 2021), and $(4Tm)_2FASn_2I_7$ (Hsu et al., 2021), is shown in Figure 4D. It is seen that the *PF* value we have achieved in $(PEA)_2SnI_4$ by SnI_4 doping is among the highest ones (Hsu et al., 2021; Yang et al., 2021). It is also notable that Sn-based OIHPs, which generally have higher σ than Pb-based OIHPs, exhibit higher *PF* values, suggesting that Sn-based OIHPs are very attractive for high-performance TE devices.

Conclusion

In conclusion, we have reported an effective doping technique by utilizing SnI_4 as a dopant for p-doping $(PEA)_2SnI_4$. The doping effect of Sn^{4+} was confirmed, and its influence on the electrical properties of $(PEA)_2SnI_4$ was revealed by electrical and spectroscopic characterizations. In addition to the doping effect, the incorporation of SnI_4 was found to improve the film morphology of $(PEA)_2SnI_4$ films. By adopting the doping technique, we were able to enhance the device performance of $(PEA)_2SnI_4$ FETs dramatically, with mobility increased from 0.25 $cm^2\ V^{-1}\ s^{-1}$ for pristine devices to 0.68 $cm^2\ V^{-1}\ s^{-1}$ for 5 mol % SnI_4-doped devices. Such performance enhancement can be attributed to the reduced contact resistance and charge trapping/scattering in the doped devices. Furthermore, we used the doping technique for improving the TE performance of $(PEA)_2SnI_4$, which shows a maximum of 3.92 $\mu W\ m^{-1}\ K^{-2}$ at a doping ratio of 5 mol %. Such a high *PF* value demonstrates the great potential of 2D Sn-based perovskite for TE applications. Overall, our work provides a viable doping technique for $(PEA)_2SnI_4$ and, more importantly, shows their promising applications in enhancing the performance of devices.

Limitations of the study

In this work, we have doped the Sn-based 2D perovskite $(PEA)_2SnI_4$ using SnI_4 as a dopant. This strategy leads to significantly improved electrical conductivity and increased crystallite size. The FET and TE devices exhibited much improved mobilities and power factors after doping with SnI_4, respectively. However, the charge scattering mechanisms in FETs at low temperatures are still unclear and require further investigations.

STAR★METHODS

Detailed methods are provided in the online version of this paper and include the following:

- KEY RESOURCES TABLE
- RESOURCE AVAILABILITY
  - Lead contact
  - Materials availability
  - Data and code availability
- METHOD DETAILS
  - Preparation of perovskite films
  - Characterization of perovskite films
  - Fabrication and characterization of FETs
  - Measurement of Seebeck coefficients

SUPPLEMENTAL INFORMATION

Supplemental information can be found online at https://doi.org/10.1016/j.isci.2022.104109.

ACKNOWLEDGMENTS

The authors thank the National Natural Science Foundation of China (62074054; U21A20497), Natural Science Foundation of Hunan Province (2019GK2245; 2020JJ1002), and Shenzhen Science and Technology Innovation Commission (RCYX20200714114537036) for financial support. The work is also supported by the Fundamental Research Funds for the Central Universities.

AUTHOR CONTRIBUTIONS

Conceptualization: Y. L. and Y. H.; Investigation: Y. L., P. C., X. Q., J. G., J. X., H. W., H. X., S. H., M. H., X. W., Z. Z. and L. L.; Writing – Original draft: Y. L. and Y. H.; Writing – Review & Editing: Y. L., L. J. and Y. H.; Supervision: L. J. and Y. H.

DECLARATION OF INTERESTS

The authors declare no competing interests.

Received: January 10, 2022
Revised: February 25, 2022
Accepted: March 14, 2022
Published: April 15, 2022

REFERENCES

Bhargava, K., and Singh, V. (2014). Electrical characterization and parameter extraction of organic thin film transistors using two dimensional numerical simulations. J. Comput. Electron. *13*, 585–592. https://doi.org/10.1007/s10825-014-0574-z.

Bi, D., Yi, C., Luo, J., Décoppet, J.-D., Zhang, F., Zakeeruddin, S.M., Li, X., Hagfeldt, A., and Grätzel, M. (2016). Polymer-templated nucleation and crystal growth of perovskite films for solar cells with efficiency greater than 21%. Nat. Energy *1*, 16142. https://doi.org/10.1038/nenergy.2016.142.

Biewald, A., Giesbrecht, N., Bein, T., Docampo, P., Hartschuh, A., and Ciesielski, R. (2019). Temperature-dependent ambipolar charge carrier mobility in large-crystal hybrid halide perovskite thin films. ACS Appl. Mater. Inter. *11*, 20838–20844. https://doi.org/10.1021/acsami.9b04592.

Buizza, L.R.V., Wright, A.D., Longo, G., Sansom, H.C., Xia, C.Q., Rosseinsky, M.J., Johnston, M.B., Snaith, H.J., and Herz, L.M. (2021). Charge-carrier mobility and localization in semiconducting Cu2AgBiI6 for photovoltaic applications. ACS Energy Lett. *6*, 1729–1739. https://doi.org/10.1021/acsenergylett.1c00458.

Cohen, B.-E., Wierzbowska, M., and Etgar, L. (2017). High efficiency and high open circuit voltage in Quasi 2D perovskite based solar cells. Adv. Funct. Mater. *27*, 1604733. https://doi.org/10.1002/adfm.201604733.

Euvrard, J., Yan, Y., and Mitzi, D.B. (2021). Electrical doping in halide perovskites. Nat. Rev. Mater. *6*, 531–549. https://doi.org/10.1038/s41578-021-00286-z.

Filippetti, A., Caddeo, C., Delugas, P., and Mattoni, A. (2016). Appealing perspectives of hybrid lead–iodide perovskites as thermoelectric materials. J. Phys. Chem. C *120*, 28472–28479. https://doi.org/10.1021/acs.jpcc.6b10278.

Gao, Y., and Dou, L. (2021). Organic semiconductor-incorporated two-dimensional halide perovskites. Natl. Sci. Rev. nwab111. https://doi.org/10.1093/nsr/nwab111.

Gao, Y., Shi, E., Deng, S., Shiring, S.B., Snaider, J.M., Liang, C., Yuan, B., Song, R., Janke, S.M., Liebman-Peláez, A., et al. (2019a). Molecular engineering of organic–inorganic hybrid perovskites quantum wells. Nat. Chem. *11*, 1151–1157. https://doi.org/10.1038/s41557-019-0354-2.

Gao, Y., Wei, Z., Yoo, P., Shi, E., Zeller, M., Zhu, C., Liao, P., and Dou, L. (2019b). Highly stable lead-free perovskite field-effect transistors incorporating linear pi-conjugated organic ligands. J. Am. Chem. Soc. *141*, 15577–15585. https://doi.org/10.1021/jacs.9b06276.

García de Arquer, F.P., Armin, A., Meredith, P., and Sargent, E.H. (2017). Solution-processed semiconductors for next-generation photodetectors. Nat. Rev. Mater. *2*, 16100. https://doi.org/10.1038/natrevmats.2016.100.

Giri, A., Chen, A.Z., Mattoni, A., Aryana, K., Zhang, D., Hu, X., Lee, S.-H., Choi, J.J., and Hopkins, P.E. (2020). Ultralow thermal conductivity of two-dimensional metal halide perovskites. Nano Lett. *20*, 3331–3337. https://doi.org/10.1021/acs.nanolett.0c00214.

Guo, H., Yang, C.-Y., Zhang, X., Motta, A., Feng, K., Xia, Y., Shi, Y., Wu, Z., Yang, K., Chen, J., et al. (2021). Transition metal-catalysed molecular n-doping of organic semiconductors. Nature *599*, 67–73. https://doi.org/10.1038/s41586-021-03942-0.

Guo, P., Stoumpos, C.C., Mao, L., Sadasivam, S., Ketterson, J.B., Darancet, P., Kanatzidis, M.G., and Schaller, R.D. (2018). Cross-plane coherent acoustic phonons in two-dimensional organic-inorganic hybrid perovskites. Nat. Commun. *9*, 2019. https://doi.org/10.1038/s41467-018-04429-9.

Hao, F., Stoumpos, C.C., Cao, D.H., Chang, R.P.H., and Kanatzidis, M.G. (2014). Lead-free solid-state organic–inorganic halide perovskite solar cells. Nat. Photon. *8*, 489–494. https://doi.org/10.1038/nphoton.2014.82.

Haque, M.A., Hernandez, L.H., Davaasuren, B., Villalva, D.R., Troughton, J., and Baran, D. (2020a). Tuning the thermoelectric performance of hybrid tin perovskites by air treatment. Adv. Energy Sustain. Res. *1*, 2000033. https://doi.org/10.1002/aesr.202000033.

Haque, M.A., Kee, S., Villalva, D.R., Ong, W.-L., and Baran, D. (2020b). Halide perovskites: thermal transport and prospects for thermoelectricity. Adv. Sci. *7*, 1903389. https://doi.org/10.1002/advs.201903389.

Haque, M.A., Nugraha, M.I., Paleti, S.H.K., and Baran, D. (2019). Role of compositional tuning on thermoelectric parameters of hybrid halide perovskites. J. Phys. Chem. C *123*, 14928–14933. https://doi.org/10.1021/acs.jpcc.9b02830.

Herz, L.M. (2017). Charge-carrier mobilities in metal halide perovskites: fundamental mechanisms and limits. ACS Energy Lett. *2*, 1539–1548. https://doi.org/10.1021/acsenergylett.7b00276.

Hsu, S.-N., Zhao, W., Gao, Y., Akriti, Segovia, M., Xu, X., Boudouris, B.W., and Dou, L. (2021). Thermoelectric performance of lead-free two-dimensional halide perovskites featuring conjugated ligands. Nano Lett. *21*, 7839–7844. https://doi.org/10.1021/acs.nanolett.1c02890.

Hu, Y., Cao, D.X., Lill, A.T., Jiang, L., Di, C.-A., Gao, X., Sirringhaus, H., and Nguyen, T.-Q. (2018a). Effect of alkyl-chain length on charge transport properties of organic semiconductors and organic field-effect transistors. Adv. Electron. Mater. *4*, 1800175. https://doi.org/10.1002/aelm.201800175.

Hu, Y., Rengert, Z.D., McDowell, C., Ford, M.J., Wang, M., Karki, A., Lill, A.T., Bazan, G.C., and Nguyen, T.-Q. (2018b). Doping polymer semiconductors by organic salts: toward high-performance solution-processed organic field-effect transistors. ACS Nano *12*, 3938–3946. https://doi.org/10.1021/acsnano.8b01460.

Jacobs, I.E., and Moule, A.J. (2017). Controlling molecular doping in organic semiconductors. Adv. Mater. *29*, 1703063. https://doi.org/10.1002/adma.201703063.

Kagan, C.R., Mitzi, D.B., and Dimitrakopoulos, C.D. (1999). Organic-inorganic hybrid materials as semiconducting channels in thin-film field-effect transistors. Science *286*, 945–947. https://doi.org/10.1126/science.286.5441.945.

Katoh, T. (1994). Temperature-independent carrier mobility in large-grain poly-Si transistors. IEEE Trans. Electron Dev. *41*, 1672–1674. https://doi.org/10.1109/16.310124.

Kim, J., Khim, D., Baeg, K.-J., Park, W.-T., Lee, S.-H., Kang, M., Noh, Y.-Y., and Kim, D.-Y. (2016). Systematic study of widely applicable N-doping strategy for high-performance solution-processed field-effect transistors. Adv. Funct. Mater. *26*, 7886–7894. https://doi.org/10.1002/adfm.201602610.

Kim, Y., Chung, S., Cho, K., Harkin, D., Hwang, W.-T., Yoo, D., Kim, J.-K., Lee, W., Song, Y., Ahn, H., et al. (2019). Enhanced charge injection properties of organic field-effect transistor by molecular implantation doping. Adv. Mater. *31*, 1806697. https://doi.org/10.1002/adma.201806697.

Liang, A., Gao, Y., Asadpour, R., Wei, Z., Finkenauer, B.P., Jin, L., Yang, J., Wang, K., Chen, K., Liao, P., et al. (2021). Ligand-Driven grain engineering of high mobility two-dimensional perovskite thin-film transistors. J. Am. Chem. Soc. *143*, 15215–15223. https://doi.org/10.1021/jacs.1c06337.

Lin, Y., Bai, Y., Fang, Y., Wang, Q., Deng, Y., and Huang, J. (2017). Suppressed ion migration in low-dimensional perovskites. ACS Energy Lett. *2*, 1571–1572. https://doi.org/10.1021/acsenergylett.7b00442.

Liu, F., Wang, L., Wang, J., Wang, F., Chen, Y., Zhang, S., Sun, H., Liu, J., Wang, G., Hu, Y., and Jiang, C. (2021). 2D Ruddlesden–popper perovskite single crystal field-effect transistors. Adv. Funct. Mater. *31*, 2005662. https://doi.org/10.1002/adfm.202005662.

Liu, Y., Chen, P.-A., and Hu, Y. (2020). Recent developments in fabrication and performance of metal halide perovskite field-effect transistors. J. Mater. Chem. C *8*. https://doi.org/10.1039/D0TC03693E.

Long, X., Pan, Z., Zhang, Z., Urban, J.J., and Wang, H. (2019). Solvent-free synthesis of organometallic halides CH3NH3PbI3 and (CH3NH3)3Bi2I9 and their thermoelectric transport properties. Appl. Phys. Lett. *115*, 072104. https://doi.org/10.1063/1.5113535.

Matsushima, T., Hwang, S., Sandanayaka, A.S., Qin, C., Terakawa, S., Fujihara, T., Yahiro, M., and Adachi, C. (2016). Solution-processed organic-inorganic perovskite field-effect transistors with high hole mobilities. Adv. Mater. *28*, 10275–10281. https://doi.org/10.1002/adma.201603126.

Mettan, X., Pisoni, R., Matus, P., Pisoni, A., Jaćimović, J., Náfrádi, B., Spina, M., Pavuna, D., Forró, L., and Horváth, E. (2015). Tuning of the thermoelectric figure of merit of CH3NH3MI3 (M=Pb,Sn) photovoltaic perovskites. J. Phys. Chem. C *119*, 11506–11510. https://doi.org/10.1021/acs.jpcc.5b03939.

Minari, T., Miyata, Y., Terayama, M., Nemoto, T., Nishinaga, T., Komatsu, K., and Isoda, S. (2006). Alkyl chain length dependent mobility of organic field-effect transistors based on thienyl-furan oligomers determined by the transfer line method. Appl. Phys. Lett. *88*, 083514. https://doi.org/10.1063/1.2179107.

Mitzi, D.B., Wang, S., Feild, C.A., Chess, C.A., and Guloy, A.M. (1995). Conducting layered organic-inorganic halides containing (110)-Oriented perovskite sheets. Science *267*, 1473–1476. https://doi.org/10.1126/science.267.5203.1473.

Ni, Z., Bao, C., Liu, Y., Jiang, Q., Wu, W.-Q., Chen, S., Dai, X., Chen, B., Hartweg, B., Yu, Z., et al. (2020). Resolving spatial and energetic distributions of trap states in metal halide perovskite solar cells. Science *367*, 1352. https://doi.org/10.1126/science.aba0893.

Qin, C., Zhang, F., Qin, L., Liu, X., Ji, H., Li, L., Hu, Y., Lou, Z., Hou, Y., and Teng, F. (2021). Charge transport in 2D layered mixed Sn–Pb perovskite thin films for field-effect transistors. Adv. Electron. Mater. *7*, 2100384. https://doi.org/10.1002/aelm.202100384.

Reo, Y., Zhu, H., Go, J.-Y., In Shim, K., Liu, A., Zou, T., Jung, H., Kim, H., Hong, J., Han, J.W., and Noh, Y.-Y. (2021). Effect of monovalent metal iodide additives on the optoelectric properties of two-dimensional Sn-based perovskite films. Chem. Mater. *33*, 2498–2505. https://doi.org/10.1021/acs.chemmater.0c04786.

Ricciarelli, D., Meggiolaro, D., Ambrosio, F., and De Angelis, F. (2020). Instability of tin iodide perovskites: bulk p-doping versus surface tin oxidation. ACS Energy Lett. *5*, 2787–2795. https://doi.org/10.1021/acsenergylett.0c01174.

Sakai, N., Warren, R., Zhang, F., Nayak, S., Liu, J., Kesava, S.V., Lin, Y.-H., Biswal, H.S., Lin, X., Grovenor, C., et al. (2021). Adduct-based p-doping of organic semiconductors. Nat. Mater. *20*, 1248–1254. https://doi.org/10.1038/s41563-021-00980-x.

Senanayak, S.P., Abdi-Jalebi, M., Kamboj, V.S., Carey, R., Shivanna, R., Tian, T., Schweicher, G., Wang, J., Giesbrecht, N., Di Nuzzo, D., et al. (2020). A general approach for hysteresis-free, operationally stable metal halide perovskite field-

effect transistors. Sci. Adv. *6*, eaaz4948. https://doi.org/10.1126/sciadv.aaz4948.

Senanayak, S.P., Yang, B., Thomas, T.H., Giesbrecht, N., Huang, W., Gann, E., Nair, B., Goedel, K., Guha, S., Moya, X., et al. (2017). Understanding charge transport in lead iodide perovskite thin-film field-effect transistors. Sci. Adv. *3*, e1601935. https://doi.org/10.1126/sciadv.1601935.

She, X.-J., Chen, C., Divitini, G., Zhao, B., Li, Y., Wang, J., Orri, J.F., Cui, L., Xu, W., Peng, J., et al. (2020). A solvent-based surface cleaning and passivation technique for suppressing ionic defects in high-mobility perovskite field-effect transistors. Nat. Electron. *3*, 1–10. https://doi.org/10.1038/s41928-020-00486-5.

Shukla, A., Sharma, V.K., Gupta, S.K., and Verma, A.S. (2020). Investigations of fundamental physical and thermoelectric properties of methylammonium lead iodide (CH3NH3PbI3) perovskites. Mater. Res. Express *6*, 126323. https://doi.org/10.1088/2053-1591/ab619b.

Stoumpos, C.C., Malliakas, C.D., and Kanatzidis, M.G. (2013). Semiconducting tin and lead iodide perovskites with organic cations: phase transitions, high mobilities, and near-infrared photoluminescent properties. Inorg. Chem. *52*, 9019–9038. https://doi.org/10.1021/ic401215x.

Takahashi, Y., Obara, R., Lin, Z.-Z., Takahashi, Y., Naito, T., Inabe, T., Ishibashi, S., and Terakura, K. (2011). Charge-transport in tin-iodide perovskite CH3NH3SnI3: origin of high conductivity. Dalton Trans. *40*, 5563–5568. https://doi.org/10.1039/C0DT01601B.

Tang, W., Zhang, J., Ratnasingham, S., Liscio, F., Chen, K., Liu, T., Wan, K., Galindez, E.S., Bilotti, E., Reece, M., et al. (2020). Substitutional doping of hybrid organic–inorganic perovskite crystals for thermoelectrics. J. Mater. Chem. A *8*, 13594–13599. https://doi.org/10.1039/D0TA03648J.

Tsai, H., Nie, W., Blancon, J.C., Stoumpos, C.C., Asadpour, R., Harutyunyan, B., Neukirch, A.J., Verduzco, R., Crochet, J.J., Tretiak, S., et al. (2016). High-efficiency two-dimensional Ruddlesden-Popper perovskite solar cells. Nature *536*, 312–316. https://doi.org/10.1038/nature18306.

Wang, J., Senanayak, S.P., Liu, J., Hu, Y., Shi, Y., Li, Z., Zhang, C., Yang, B., Jiang, L., Di, D., et al. (2019a). Investigation of electrode electrochemical reactions in CH3 NH3 PbBr3 perovskite single-crystal field-effect transistors. Adv. Mater. *31*, e1902618. https://doi.org/10.1002/adma.201902618.

Wang, R., Mujahid, M., Duan, Y., Wang, Z.K., Xue, J., and Yang, Y. (2019b). A review of perovskites solar cell stability. Adv. Funct. Mater. *29*, 1808843. https://doi.org/10.1002/adfm.201808843.

Wei, H., Chen, P.-A., Guo, J., Liu, Y., Qiu, X., Chen, H., Zeng, Z., Nguyen, T.-Q., and Hu, Y. (2021). Low-cost nucleophilic organic bases as n-dopants for organic field-effect transistors and thermoelectric devices. Adv. Funct. Mater. *31*, 2102768. https://doi.org/10.1002/adfm.202102768.

Wright, A.D., Verdi, C., Milot, R.L., Eperon, G.E., Pérez-Osorio, M.A., Snaith, H.J., Giustino, F., Johnston, M.B., and Herz, L.M. (2016). Electron–phonon coupling in hybrid lead halide perovskites. Nat. Commun. *7*, 11755. https://doi.org/10.1038/ncomms11755.

Wu, P., Xiong, Y., Sun, L., Xie, G., and Xu, L. (2018). Enhancing thermoelectric performance of the CH3NH3PbI3 polycrystalline thin films by using the excited state on photoexcitation. Org. Electron. *55*, 90–96. https://doi.org/10.1016/j.orgel.2018.01.014.

Xie, Z., Feng, K., Xiong, Y., Chen, X., Liang, Y., Abid, K., and Xu, L. (2021). A high seebeck voltage thermoelectric module with P-type and N-type MAPbI3 perovskite single crystals. Adv. Electron. Mater. *7*, 2001003. https://doi.org/10.1002/aelm.202001003.

Xiong, Y., Xu, L., Wu, P., Sun, L., Xie, G., and Hu, B. (2019). Bismuth doping–induced stable Seebeck effect based on MAPbI3 polycrystalline thin films. Adv. Funct. Mater. *29*, 1900615. https://doi.org/10.1002/adfm.201900615.

Xu, Y., Gwoziecki, R., Chartier, I., Coppard, R., Balestra, F., and Ghibaudo, G. (2010). Modified transmission-line method for contact resistance extraction in organic field-effect transistors. Appl. Phys. Lett. *97*, 063302. https://doi.org/10.1063/1.3479476.

Yamashita, Y., Tsurumi, J., Ohno, M., Fujimoto, R., Kumagai, S., Kurosawa, T., Okamoto, T., Takeya, J., and Watanabe, S. (2019). Efficient molecular doping of polymeric semiconductors driven by anion exchange. Nature *572*, 634–638. https://doi.org/10.1038/s41586-019-1504-9.

Yang, S.J., Kim, D., Choi, J., Kim, S.H., Park, K., Ryu, S., and Cho, K. (2021). Enhancing thermoelectric power factor of 2D organometal halide perovskites by suppressing 2D/3D phase separation. Adv. Mater. *33*, 2102797. https://doi.org/10.1002/adma.202102797.

Ye, T., Wang, X., Li, X., Yan, A.Q., Ramakrishna, S., and Xu, J. (2017). Ultra-high Seebeck coefficient and low thermal conductivity of a centimeter-sized perovskite single crystal acquired by a modified fast growth method. J. Mater. Chem. C *5*, 1255–1260. https://doi.org/10.1039/C6TC04594D.

Yi, H.T., Wu, X., Zhu, X., and Podzorov, V. (2016). Intrinsic charge transport across phase transitions in hybrid organo-inorganic perovskites. Adv. Mater. *28*, 6509–6514. https://doi.org/10.1002/adma.201600011.

Zeidell, A.M., Tyznik, C., Jennings, L., Zhang, C., Lee, H., Guthold, M., Vardeny, Z.V., and Jurchescu, O.D. (2018). Enhanced charge transport in hybrid perovskite field-effect transistors via microstructure control. Adv. Electron. Mater. *4*, 1800316. https://doi.org/10.1002/aelm.201800316.

Zhang, F., Zhang, H., Zhu, L., Qin, L., Wang, Y., Hu, Y., Lou, Z., Hou, Y., and Teng, F. (2019). Two-dimensional organic–inorganic hybrid perovskite field-effect transistors with polymers as bottom-gate dielectrics. J. Mater. Chem. C *7*, 4004–4012. https://doi.org/10.1039/c8tc06249h.

Zhang, F., Zhang, Q., Liu, X., Hu, Y., Lou, Z., Hou, Y., and Teng, F. (2021). Property modulation of two-dimensional lead-free perovskite thin films by aromatic polymer additives for performance enhancement of field-effect transistors. ACS Appl. Mater. Inter. *13*, 24272–24284. https://doi.org/10.1021/acsami.1c03041.

Zhao, B., Lian, Y., Cui, L., Divitini, G., Kusch, G., Ruggeri, E., Auras, F., Li, W., Yang, D., Zhu, B., et al. (2020). Efficient light-emitting diodes from mixed-dimensional perovskites on a fluoride interface. Nat. Electron. *3*, 1–7. https://doi.org/10.1038/s41928-020-00487-4.

Zhu, H., Liu, A., Kim, H., Hong, J., Go, J.-Y., and Noh, Y.-Y. (2020a). High-performance layered perovskite transistors and phototransistors by binary solvent engineering. Chem. Mater. *33*, 1174–1181. https://doi.org/10.1021/acs.chemmater.0c03822.

Zhu, H., Liu, A., Shim, K.I., Hong, J., Han, J.W., and Noh, Y.-Y. (2020b). High-performance and Reliable lead-free layered-perovskite transistors. Adv. Mater. *32*, 2002717. https://doi.org/10.1002/adma.202002717.

STAR★METHODS

KEY RESOURCES TABLE

REAGENT or RESOURCE	SOURCE	IDENTIFIER
Chemicals, peptides, and recombinant proteins		
Phenethylammonium Iodide, ≥99.5%	Xi'an Polymer	Cat#PLT501391I
Tin(II) iodide, AnhydroBeads™, −10 mesh, 99.99% trace metals basis	Aldrich	Cat#409308
N,*N*-Dimethylformamide, anhydrous, 99.8%	Aldrich	Cat#227056
1-Methyl-2-pyrrolidinone, anhydrous, 99.5%, packaged under Argon in resealable ChemSealTM bottles	Alfa Aesar	Cat#043741
Tin(IV) iodide ,95%	Aladdin	Cat#T195042
Other		
Keithley 4200 semiconductor analyzer	Tektronix Technologies	https://www.tek.com/en/keithley-4200a-scs-parameter-analyzer
Axis Supra spectrometer	Kratos	https://www.kratos.com/products/axis-supra-xps-surface-analysis-instrument
MIRA3 SEM	TESCAN	http://www.tescan-china.com/zh-cn/technology/special-solutions/mira3-amu
Park XE-7 AFM	Park Systems	https://parksystems.com/products/small-sample-afm/park-xe7/overview
D/max 2550 XRD	Rigaku	https://www.directindustry-china.cn/prod/rigaku/product-31512-886693.html
UV-3600 PLUS	SHIMADZU	https://shimadzu.com.au/uv-3600-plus
B2912A Precision Sources	Keysight	https://www.keysight.com/us/en/product/B2912A/precision-source-measure-unit-2-ch-10fa-210v-3a-dc-10-5a-pulse.html?rd=1
ST-100 cryostat	Janis	https://www.lakeshore.com/products/product-detail/janis/st-100-optical-cryostat

RESOURCE AVAILABILITY

Lead contact

Further information and requests for resources and reagents should be directed to and will be fulfilled by the lead contact, Yuanyuan Hu (yhu@hnu.edu.cn).

Materials availability

This study did not generate new unique reagents.

Data and code availability

Any additional information required to reanalyze the data reported in this paper is available from the lead contact upon request.

METHOD DETAILS

Preparation of perovskite films

Sn^{4+} was introduced by mixing PEAI, SnI_2 and SnI_4 with mol ratio of 2:1−*x*:*x* (0 < *x* < 1) in a mixture of DMF and NMP with volume ratio of 3:1, where *x* represents the doping ratio of SnI_4. 0.1 M $(PEAI)_2(SnI_2)_{1-x}(SnI_4)_x$ precursor solutions were formed by heating at 60°C for 4 h in an Ar-filled glove box. Then, the precursor solutions were stored for 1 h to cool down to room temperature naturally and filtered through 0.45 μm

polytetrafluoroethylene (PTFE) filters. Glass or Si^{++}/SiO_2 substrates were cleaned sequentially by deionized water, acetone and isopropanol, and blown dry by nitrogen gas. The substrates were treated with UV/ozone for 30 min before use. Perovskite films were prepared by spin-coating the precursor solution on the substrates at 4000 rpm for 30 s and annealing at 100°C for 10 min in an Ar-filled glove box.

Characterization of perovskite films

For electrical conductivity measurements, the perovskite films were deposited on SiO_2 substrates with pre-defined electrodes (Cr/Au, 2 nm/30 nm). The conductivity of the prepared devices was measured using a probe station in an Ar glove box by four-point probe method through a Keithley 4200 semiconductor analyzer. XPS and UPS measurements were carried out by a Kratos Axis Supra spectrometer under a high vacuum. The morphologies of the films were investigated by SEM (MIRA3, TESCAN). The thicknesses of the films were measured by atomic force microscopy (AFM) (Park XE-7). The XRD patterns were recorded by D/max 2550 (Rigaku) under Cu Kα (λ = 1.5406 Å) irradiation. The steady PL spectra were recorded by a Thermo Scientific Lumina. The time-resolved PL measurements were performed using a confocal microscope (WITec, alpha-300) as the collect device, and the emission signal was reflected into a streak camera (C10910, Hamamatsu) by Ag mirrors. The laser beam (405 nm) was focused on the sample with a spot diameter of ≈3 μm from the top by an objective lens (50×, Zeiss, 0.75 NA), while PL emission was collected by the same objective lens. The ultraviolet-visible-near-infrared (UV-vis-NIR) absorption spectra of solution and film samples were measured with UV-3600 PLUS (SHIMADZU).

Fabrication and characterization of FETs

This study did not generate new unique reagents. Si^{++}/SiO_2 substrates with bottom-contact electrodes (Cr/Au: 2 nm/30 nm) defined by photolithography were cleaned sequentially by deionized water, acetone and isopropanol, and blown dry by nitrogen gas. The substrates were treated with UV/ozone for 30 min before use. The BGBC FETs were fabricated by spin-coating perovskite precursors on the SiO_2 substrates at 4000 rpm for 30 s and annealing at 100°C for 10 min in an Ar-filled glove box. The transistor electrical characteristics at RT (about 25 °C) and in the dark were collected immediately after preparation using a probe station in an Ar-filled glove box through a Keysight B2912A Precision Sources in DC mode. For the temperature-dependent measurement, the device was loaded into a Janis ST-100 cryostat in an Ar-filled glove box, and the electrical measurements were taken in vacuum with pressure lower than 1×10^{-5} mbar. All measurement processes were carried out under dark conditions. The saturation FET mobility was calculated from both forward and backward curves using

$$\mu_{sat} = \frac{2L}{WC_i}\left(\frac{\partial\sqrt{|I_{DS}|}}{\partial\sqrt{|V_{GS}|}}\right)^2$$

where L, W and C_i are the channel length, width, and dielectric area capacitance, respectively.

Measurement of Seebeck coefficients

Thermoelectric devices were fabricated by the same spin-coating process on the cleaned glass substrates. To measure the Seebeck coefficients of doped $(PEA)_2SnI_4$ films, a homemade thermoelectric measurement system was used. The devices containing one heater, two thermometers which also act as electrical contacts were fabricated by photolithographic patterning of metal bilayers of Cr (10 nm) and Au (15 nm) on glass substrates. To obtain Seebeck coefficient $S = \Delta V/\Delta T$, the temperature gradient between the two electrodes was estimated by converting the resistance of electrodes into temperature using the temperature-coefficient-of resistance (TCR), and the built-in thermal voltage was measured using Keithley Nanovoltmeter model 2182A. All Seebeck coefficients were measured at RT in a high vacuum ($<10^{-5}$ mbar) using Janis ST-100 in the dark.